ON CONTROLLING NONLINEAR DISSIPATION IN HIGH ORDER FILTER METHODS FOR IDEAL AND NON-IDEAL MHD

H. C. YEE

NASA Ames Research Center, Moffett Field, Calif., 94035, USA

AND

B. SJÖGREEN

The Royal Institute of Technology, 100 44 Stockholm, Sweden

Abstract: The newly developed adaptive numerical dissipation control in spatially high order filter schemes [20] [16] for the compressible Euler and Navier-Stokes equations has been recently extended to the ideal and non-ideal magnetohydrodynamics (MHD) equations [17, 24, 23, 25]. These filter schemes are applicable to complex unsteady MHD high-speed shock/shear/turbulence problems. They also provide a natural and efficient way for the minimization of $\mathbf{Div(B)}$ numerical error [23, 24]. The adaptive numerical dissipation mechanism consists of automatic detection of different flow features as distinct sensors to signal the appropriate type and amount of numerical dissipation/filter where needed and leave the rest of the region free from numerical dissipation contamination. The numerical dissipation considered consists of high order linear dissipation for the suppression of high frequency oscillation and the nonlinear dissipative portion of high-resolution shock-capturing methods for discontinuity capturing. The applicable nonlinear dissipative portion of high-resolution shock-capturing methods is very general. The objective of this paper is to investigate the performance of three commonly used types of nonlinear numerical dissipation for both the ideal and non-ideal MHD.

1. A New Method in Solving the Multi-Dimensional Conservative MHD Equations

Consider the 3-D conservative and non-conservative (symmetrizable [6, 14]) forms of the ideal compressible MHD equations in Cartesian grids,

$$
\begin{pmatrix} \rho \\ \rho u \\ \rho v \\ \rho w \\ e \\ B_x \\ B_y \\ B_z \end{pmatrix}_t + \operatorname{div} \begin{pmatrix} \rho \mathbf{u} \\ \rho \mathbf{u}\mathbf{u}^T + (p + B^2/2)I - \mathbf{B}\mathbf{B}^T \\ \mathbf{u}(e + p + B^2/2) - \mathbf{B}(\mathbf{u}^T\mathbf{B}) \\ \mathbf{u}\mathbf{B}^T - \mathbf{B}\mathbf{u}^T \end{pmatrix} = 0 \quad \text{(conservative)}, \tag{1.1}
$$

and

$$
\begin{pmatrix} \rho \\ \rho u \\ \rho v \\ \rho w \\ e \\ B_x \\ B_y \\ B_z \end{pmatrix}_t + \mathrm{div} \begin{pmatrix} \rho \mathbf{u} \\ \rho \mathbf{u}\mathbf{u}^T + (p + B^2/2)I - \mathbf{B}\mathbf{B}^T \\ \mathbf{u}(e + p + B^2/2) - \mathbf{B}(\mathbf{u}^T\mathbf{B}) \\ \mathbf{u}\mathbf{B}^T - \mathbf{B}\mathbf{u}^T \end{pmatrix} = -(\nabla \cdot \mathbf{B}) \begin{pmatrix} 0 \\ B_x \\ B_y \\ B_z \\ \mathbf{u}^T\mathbf{B} \\ u \\ v \\ w \end{pmatrix} \quad \text{(non-conservative)},
$$

$$(1.2)$$

where the velocity vector $\mathbf{u} = (u, v, w)^T$, the magnetic field vector $\mathbf{B} = (B_x, B_y, B_z)^T$, ρ is the density, and e is the total energy. The notation $B^2 = B_x^2 + B_y^2 + B_z^2$ is used. The pressure is related to the other variables by

$$
p = (\gamma - 1)(e - \frac{1}{2}\rho(u^2 + v^2 + w^2) - \frac{1}{2}(B_x^2 + B_y^2 + B_z^2)).
$$

For plasmas and monatomic gases, $\gamma = 5/3$. The vector on the right hand side of (1.2) is the non-conservative portion of the symmetrizable MHD equations and is frequently referred to in the literature as a source term vector. The authors prefer not to use this nomenclature since this is part of the symmetrizable form of the MHD and it is not a source term.

The conservative and non-conservative forms can be written as

$$
U_t + \nabla \cdot \mathbf{F} = 0,
$$

$$
U_t + \nabla \cdot \mathbf{F} = S,
$$

respectively, where U is the state vector, $\mathbf{F}$ is the conservative inviscid flux vector tensor and S is the non-conservative portion of the equations in (1.2). The conservative and non-conservative forms of the non-ideal compressible MHD [5] takes the form

$$
U_t + \nabla \cdot \mathbf{F} = \mathbf{F}_v,
$$

$$
U_t + \nabla \cdot \mathbf{F} = \mathbf{F}_v + S,
$$

$$
\mathbf{F}_v = [\, 0 \quad \mathrm{div}\tau \quad \mathrm{div}(\mathbf{u}^T\tau) + \mathrm{div}\mathbf{h} - \frac{1}{\sigma}\mathrm{div}((\nabla \times \mathbf{B}) \times \mathbf{B}) \quad \frac{1}{\sigma}(\triangle \mathbf{B} - \nabla \mathrm{div}\mathbf{B})\,]^T.
$$

The vector $\mathbf{F}_v$ includes viscosity, resistivity, and conductivity with τ being the viscous stress tensor, σ the resistivity coefficient, and $\mathbf{h}$ the heat flux.

2. Solving the Conservative System Using the Non-Conservative Eigenvectors

Our adaptive numerical dissipation mechanism consists of automatic detection of different flow features as distinct sensors to signal the appropriate type and amount of numerical dissipation/filter where needed and leave the rest of the region free from numerical dissipation contamination. An important ingredient in our method is the use of the dissipative portion of high-resolution shock-capturing schemes as part of the nonlinear filters for discontinuity capturing. If the dissipative portion of higher order Lax-Friedrichs or Nessyahu-Tadmor [9] type of shock-capturing schemes are not employed (see [19, 20] for a discussion), these nonlinear filters usually involve the use of approximate Riemann solvers. Due to the fact that the inviscid fluxes of the 2-D and 3-D conservative MHD systems do not have a complete set of eigenvectors, we will, therefore, first discuss a new form of high-resolution shock-capturing schemes for the conservative MHD equations using the non-conservative eigensystem [17, 24].

For non-ideal MHD, we apply the inviscid MHD base scheme twice for the viscous flux derivatives. There is no viscous filtering involved. In addition, without lost of generality, we will describe our numerical methods for the inviscid x-flux of the ideal MHD (1.1) on a uniform grid. The schemes to be discussed, in most part, only spell out the x-component terms with the y- and z-components omitted. Let $A(U)$ denote the Jacobian $\partial F/\partial U$ with the understanding that the present F and S are the inviscid x-component of the 3-D description above. For later discussion we write the non-conservative term S, in the x-direction as $N(U)U_x$.

Seven of the eigenvalues and eigenvectors are identical for the "conservative" Jacobian matrix A and the "non-conservative" Jacobian matrix $(A - N)$ [4, 1]. For ease of reference, we refer to the distinct eigenvalue (eigenvector) between the conservative and non-conservative MHD as the eighth eigenvalue (eigenvector). The eighth eigenvector of A of the conservative system associated with the degenerate zero eigenvalue can sometimes coincide with one of the other eigenvectors, thereby, making it difficult to obtain the Roe-type approximate Riemann solver for the multi-dimensional conservative MHD. On the other hand, the eigenvectors of the non-conservative Jacobian $A^* = (A - N)$ always form a complete basis, and can be obtained from analytical formulas [6, 14] for 1-D or higher. A Roe-type average state was developed in [1] for the 8-wave 1-D conservative MHD and extended to the 3-D non-conservative MHD by Gallice [4].

In [17, 24, 23], we proposed to use eigenvectors of the non-conservative form but with the degenerate eigenvalue replaced by an entropy correction [7, 19] (a small parameter ϵ that is scaled by the largest eigenvalue of $A(U)$) for the conservative form. For more than one-space dimension, a multi-dimension entropy correction as proposed in [19] is used for each of the degenerate eigenvalues in each spatial direction. Our rationale for doing this is that the incorrect eigenvector for the conservative form will be multiplied by an eigenvalue which is close to zero. Thus the effect of a "false" eigenvector will be small. Note that in the present context, the use of the an entropy correction is different from the standard entropy correction associated with expansion shocks in the Roe-type approximate solver in gas dynamics [7, 19], since the conservative inviscid gas dynamics equations are strictly hyperbolic.

3. Description of High Order Filter Methods

Our filter idea is very general and can be used in conjunction with spectral, compact and non-compact spatially central base schemes. Basically, the filter method consists of two steps, a divergence-free preserving (base scheme) step (not involving the use of approximate Riemann solvers or flux limiters) and a filter step (usually involving the use of approximate Riemann solvers and flux limiters). In order to have good shock-capturing capability and improved non-linear stability related to spurious high frequency oscillations, the blending of a high order non-linear filter and a high order linear filter was proposed in [22, 24]. The nonlinear filter consists of the **product** of an artificial compression method (ACM) indicator or wavelet sensor and the nonlinear dissipative portion of a high-resolution shock-capturing scheme. The high order linear filter consists of the product of another sensor, a tuning parameter and a high order centered linear dissipative operator that is compatible with the order of the base scheme being used. Here the extension with a modification of the gas dynamic filter approach to the MHD equations that minimizes the $\nabla \cdot B$ numerical error is summarized. Due to space limitation, only the nonlinear filter using wavelets as sensors is presented here. The numerical examples considered exhibit highly accurate solutions without the use of high order linear filters.

3.1. DIVERGENCE-FREE PRESERVING BASE SCHEME STEP

The first step of the numerical method consists of a time step via a high order non-dissipative spatial and high order temporal base scheme operator L^*. After the completion of a full time

step of the base scheme step, the solution is denoted by U^*

$$U^* = L^*(U^n),$$ (3.3)

where U^n is the numerical solution vector at time level n. For example, a spatially divergence-free preserving eighth-order linear dissipation with the sixth-order centered base scheme to approximate $F(U)_x$ is written as (with the grid indices k and l for the y- and z-directions suppressed)

$$\frac{\partial F}{\partial x} \approx D_{06}F_j + d(\Delta x)^7(D_+D_-)^4U_j,$$ (3.4)

where D_{06} is the standard sixth-order accurate centered difference operator, and D_+D_- is the standard second-order accurate centered approximation of the second derivative. The small parameter d is a scaled value in the range of 0.00001 to 0.01, depending on the flow problem, and has the sign which gives dissipation in the forward time direction. The D_{06} operator is modified at boundaries in a stable way by the so called summation-by-part (SBP) operators [11, 10, 22]. The linear numerical dissipation operator D_+D_- is modified at the boundaries to be semi-bounded [15]. The base scheme step with the fourth-order classical Runge-Kutta time discretization takes the form

$$
\begin{aligned}
k_1 &= L(U^n) \\
k_2 &= L(U^n + \tfrac{\Delta t}{2}k_1) \\
k_3 &= L(U^n + \tfrac{\Delta t}{2}k_2) \\
k_4 &= L(U^n + \Delta t k_3) \\
U^* &= U^n + \tfrac{\Delta t}{6}[k_1 + 2k_2 + 2k_3 + k_4] = L^*(U^n),
\end{aligned}
$$ (3.5)

where the L operator is a semi-discrete form of the conservative system (1.1) or non-conservative system (1.2). For example, using formula (3.4) to discretize (1.1) with the flux tensor $\mathbf{F} = (F, G, H)$ takes the form

$$
\begin{aligned}
\frac{d(U_{j,k,l})}{dt} &= L(U)_{j,k,l} \\
&= -\{(D_j)_{06}F_{j,k,l} + (d_x)(\Delta x)^7[(D_j)_+(D_j)_-]^4 U_{j,k,l} \\
&\quad + (D_k)_{06}G_{j,k,l} + (d_y)(\Delta y)^7[(D_k)_+(D_k)_-]^4 U_{j,k,l} \\
&\quad + (D_l)_{06}H_{j,k,l} + (d_z)(\Delta z)^7[(D_l)_+(D_l)_-]^4 U_{j,k,l}\},
\end{aligned}
$$ (3.6)

where D_j, D_k and D_l denote finite difference operators acting in the j-, k-, l-directions, respectively. Here, e.g., $(D_j)_{06}$ denotes the sixth-order centered difference operator in the x-direction. Similarly, $(D_j)_+(D_j)_-$ denotes the second-order centered approximation of the second derivative in the j-direction. The small parameters d_x, d_y and d_z are the same as d in (3.4). This highly accurate spatial base scheme is employed to numerically preserve the divergence-free condition of the magnetic field (to the level of round-off error) for uniform Cartesian grids with periodic boundary conditions.

3.2. ADAPTIVE NUMERICAL DISSIPATION FILTER STEP

After the completion of a full time step of the divergence-free preserving base scheme step, the second step is to adaptively filter the solution by the **product** of a "wavelet sensor" and the "**nonlinear dissipative portion** of a high-resolution shock-capturing scheme". If necessary, the blending of a high order linear filter with a nonlinear filter [22] can be employed and not discuss here. The final update step after the filter step can be written as (with some of grid indices suppressed for ease of illustration)

$$U_{j,k,l}^{n+1} = U_{j,k,l}^* - \frac{\Delta t}{\Delta x}[H_{j+1/2}^{fx} - H_{j-1/2}^{fx}] - \frac{\Delta t}{\Delta y}[H_{k+1/2}^{fy} - H_{k-1/2}^{fy}] - \frac{\Delta t}{\Delta z}[H_{l+1/2}^{fz} - H_{l-1/2}^{fz}]. \quad (3.7)$$

Here, $H_{j\pm1/2}^{fx}$, $H_{k\pm1/2}^{fy}$ and $H_{l\pm1/2}^{fz}$ are the filter numerical fluxes in the x, y and z-directions, respectively. The x-filter numerical flux vector $H_{j+1/2}^{fx}$ (with the y- and z-components grid indices suppressed) is

$$H_{j+1/2}^{fx} = R_{j+1/2}\overline{H}_{j+1/2},$$

where $R_{j+1/2}$ is the matrix of right eigenvectors of the Jacobian of the non-conservative MHD flux vector $(A_{j+1/2} - N_{j+1/2})$ evaluated at the Gallice average state [4] in terms of the U^* solution from the base scheme step (3.3). The notation $R_{j+1/2}$ stands for $R_{j+1/2,k,l}$ and the subscript in $R_{j+1/2}$ indicates the average state evaluated in the x-direction of the eigenvectors in terms of U^*. See [4] or Appendix A of [24] for the average state formula for the 3-D non-conservative system (1.2). The $\overline{H}_{j+1/2}$ (involving the use of wavelet sensors and flux limiters) are also evaluated from the same average state. The dimension-by-dimension procedure of applying the approximate Riemann solver is adopted.

Denote the elements of the vector $\overline{H}_{j+1/2}$ by $\overline{h}_{j+1/2}^l$, $l = 1, 2, ..., 8$. The nonlinear portion of the filter $\overline{h}_{j+1/2}^l$, $l = 1, 2, ..., 8$, has the form

$$\overline{h}_{j+1/2}^l = \frac{1}{2}(s^N)_{j+1/2}^l(\phi_{j+1/2}^l). \quad (3.8)$$

Here $(s^N)_{j+1/2}^l$ is the sensor to activate the higher order nonlinear numerical dissipation filter. For example, $(s^N)_{j+1/2}^l$ is designed to be zero or near zero in regions of smooth flow and near one in regions with discontinuities. $(s^N)_{j+1/2}^l$ varies from one grid point to another and is obtained from a wavelet analysis of the flow solution [16]. The function $\phi_{j+1/2}^l$ is the dissipative portion of the nonlinear filter for the local lth-characteristic wave [22] in the x-direction. Note that the wavelet sensor can be obtained from the characteristic variables for each wave or a single sensor for all eight waves, based on pressure and density. Both methods were implemented but for the numerical test in this paper, the simpler non-characteristic sensor was employed.

The dissipative portion of the nonlinear filter $\phi_{j+1/2}^l = g_{j+1/2}^l - b_{j+1/2}^l$ is the dissipative portion of a high order high-resolution shock-capturing scheme for the local lth-characteristic wave. Here $g_{j+1/2}^l$ and $b_{j+1/2}^l$ are numerical fluxes of the uniformly high order high-resolution scheme and a high order central scheme for the lth characteristic, respectively. It is noted that $b_{j+1/2}^l$ might not be unique since there is more than one way of obtaining $\phi_{j+1/2}^l$.

Three forms of nonlinear dissipation $\phi_{j+1/2}^l$ are considered, namely:

- Dissipative portion of the fifth-order WENO scheme (WENO5) [8]. It can be obtained e.g., in the x-direction by taking the full WENO5 scheme in the x-direction and subtracting $D_{06}F_j$.
- Dissipative portion of the a second-order MUSCL scheme [20].
- Dissipative portion of the Harten-Yee TVD scheme [20, 24].

For example, the forms of Harten and Yee and symmetric TVD schemes [19] are already in the proper form in the sense that they are written in a central differencing portion $b_{j+1/2}^l$ and a nonlinear dissipation portion $\phi_{j+1/2}^l$. No work is required to obtain $\phi_{j+1/2}^l$ in this case.

The nonlinear filter given by (3.8), if applied to the entire MHD system, will not preserve the divergence free magnetic field condition in general. For the computations in this paper, the "No

filter on B" option is chosen. The nonlinear filter step of (3.8) only acts on the gas dynamic portion of the equations. That is, the nonlinear filter step (3.8) only applies to the first five equations of (1.1) or (1.2). Here the complete set of eigenvalues and eigenvectors of the full non-conservative MHD system is used to evaluate the first five equations of (1.1) or (1.2). With the divergence free spatial base scheme, the divergence free property should be preserved. Extensive grid convergence comparison of the "no filter on B" with the "filter all of the MHD equations" (filter all) options were presented in [24]. Alternative approaches in obtaining divergence-free preserving shock-capturing filters follow in a similar vein as the constrained transport approach [3] or the projection method [26].

4. 2-D Compressible Ideal and Non-ideal MHD Numerical Examples

The wavelet filter schemes using the dissipative portion of WENO5, second-order MUSCL and Harten-Yee TVD schemes with sixth-order spatial central base scheme ($d = 0$ in (3.4)) for both the inviscid and viscous MHD flux derivatives and a fourth-order Runge-Kutta method are denoted by WAV66weno5, WAV66mus and WAV66hy respectively. The first number indicates the order of the base scheme for discretizing the inviscid flux derivatives. The second number indicates the order of the scheme for discretizing the viscous flux derivatives, if present. As mentioned before, there is no filtering for the viscous fluxes. If an eighth-order linear dissipation ($d \neq 0$ in (3.4)) is used for the base scheme, the symbol "AD8" is added as in WAV66weno5+AD8. Computation using the same temporal and spatial scheme for the viscous MHD flux derivatives, and the standard fifth-order WENO scheme for the inviscid flux derivatives is denoted by WENO5. Computations using a second-order MUSCL and the Harten-Yee [24] TVD scheme for the inviscid MHD flux with the second-order central scheme for the viscous flux and a second-order Runge-Kutta method are denoted by MUSCL and HY, respectively.

The entropy fix parameter ϵ is 0.25 for the Harten-Yee, MUSCL, WAV66mus and WAV66hy schemes (to avoid expansion shocks and carbuncle phenomenon). The cut off wavelet Lipschitz exponent β is 0.5 [16] for all the wavelet filter schemes. See [20, 16, 22] or Appendix B of [24] for the definition of ϵ and β. Except for WENO5, the van Leer version of the van Albada limiter is used. For the second-order MUSCL scheme, the limiter is applied to the primitive variables. For viscous computations, the Reynolds number $Re = 1000$, resistivity coefficient of 100 and a Prantdl number of 0.72 are used for all test cases. Extensive grid convergence studies using WAV66hy and ACM66hy (using ACM instead of wavelet as the sensor) for typical ideal and non-ideal MHD test cases were conducted in [17, 24, 25]. More accurate solutions were obtained with WAV66hy and ACM66hy than with WENO5, which is more CPU intensive. The following investigates the performance of the three different filters.

4.1. COMPRESSIBLE MHD ORSZAG-TANG VORTEX ($\gamma = 5/3$, PERIODIC BC)

The 2-D Compressible MHD Orszag-Tang vortex problem [12, 13, 2] consists of periodic boundary conditions with smooth initial data .

$$(\rho,\ u,\ v,\ w,\ p,\ B_x,\ B_y,\ B_z) = (25/9,\ -\sin y,\ \sin x,\ 0,\ 5/3,\ -\sin y,\ \sin 2x,\ 0).$$

The initial sine waves break into discontinuities at a later time with complicated flow interactions. The computational domain is $0 < x < 2\pi$, $0 < y < 2\pi$ and the computation stops at time T= 3.14 ($\approx \pi$), when discontinuities have formed and interacted. The solution has both complicated structure and discontinuities. Density contours with 30 equally spaced contours between 0.9 and 6.1 are used for illustration.

Figures 1 and 2 show the comparison among the three filter schemes (no filter on **B** option), WENO5, MUSCL and Harten-Yee (HY) using uniform 101×101 and 801×801 grids for the inviscid MHD. Figures 3 and 4 show the corresponding viscous MHD comparison.
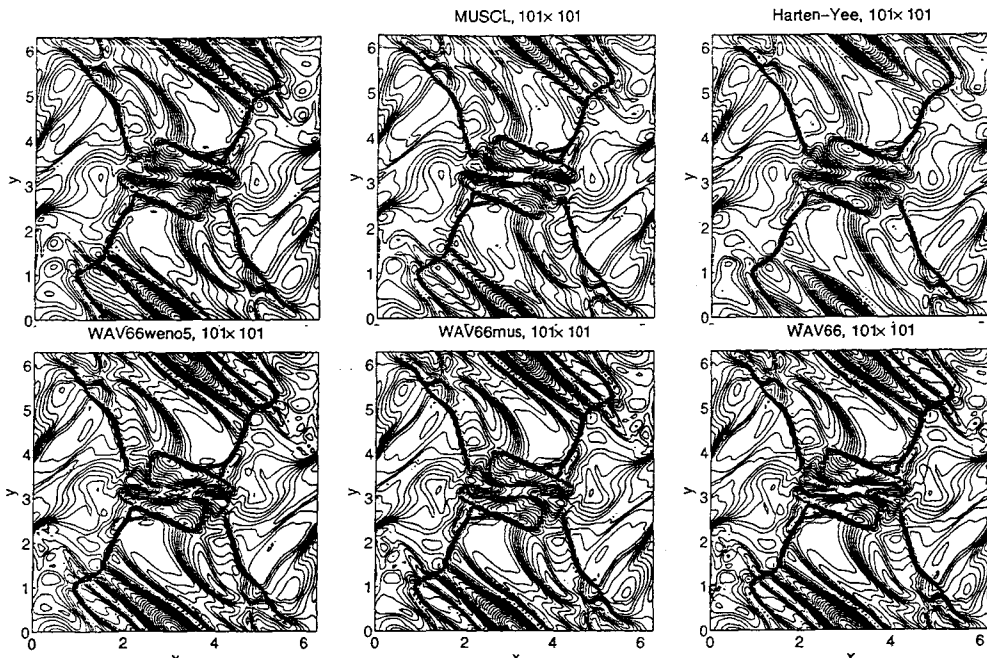
MUSCL, 101× 101   Harten–Yee, 101× 101

WAV66weno5, 101× 101   WAV66mus, 101× 101   WAV66, 101× 101

Fig. 1. *Inviscid Orszag-Tang Problem using a* 101 × 101 *grid. Density contours for the ideal MHD at* $T = 3.14$. *Top row: WENO5(left), MUSCL(middle), HY(right). Bottom row: WAV66weno5(left), WAV66mus(middle), WAV66hy(right).*
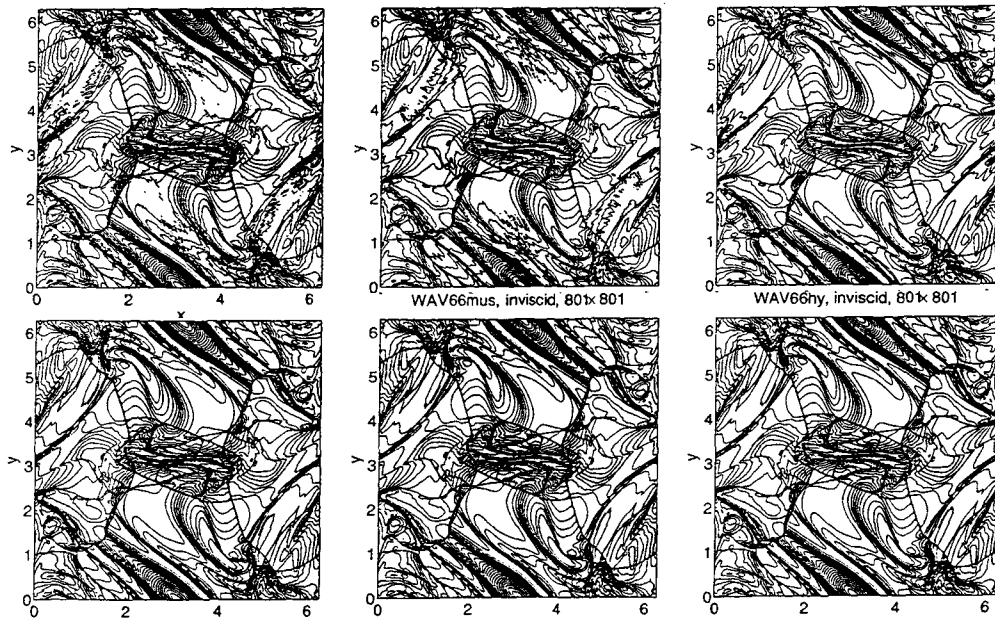
WAV66mus, inviscid, 80× 801   WAV66hy, inviscid, 80× 801

Fig. 2. *Inviscid Orszag-Tang Problem using a* 801 × 801 *grid. Density contours for the ideal MHD at* $T = 3.14$. *Top row: WENO5(left), MUSCL(middle), HY(right). Bottom row: WAV66weno5(left), WAV66mus(middle), WAV66hy(right).*

Convergence solutions were obtained by all six methods using the 801 × 801 grid. Computations based on a 1601 × 1601 grids are used as the reference solutions. For 51 × 51 and 101 × 101 grids, small structures are more well captured by the three filter methods than that of WENO5, MUSCL and Harten-Yee. In addition, for the inviscid case, the three filter methods are more stable than that of the other three methods in the sense larger CFL number can be used. Figure 2 shows the computations using a CFL of 0.6 and a 801 × 801 grid. WENO5 and MUSCL show a slight small oscillation. By applying the limiter in the characteristic variables in the MUSCL scheme these oscillations are suppressed.
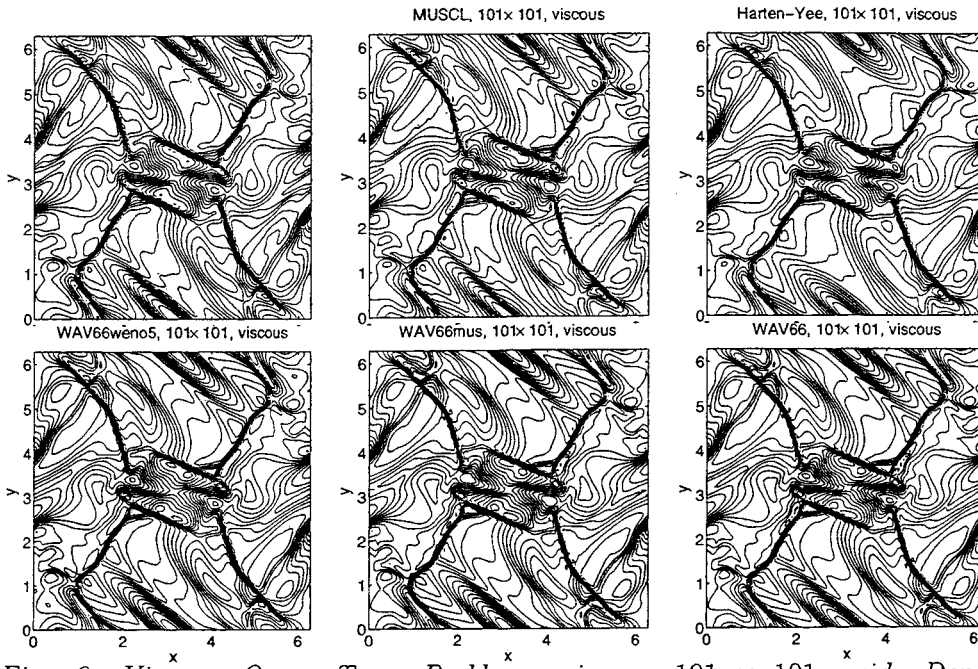
Fig. 3. *Viscous Orszag-Tang Problem using a* 101×101 *grid. Density contours for non-ideal MHD with* $Re = 1000$, *and resistivity coeff. of* 100 *at* $T = 3.14$. *Top row: WENO5(left), MUSCL(middle), HY(right). Bottom row: WAV66weno5(left), WAV66mus(middle), WAV66hy(right).*
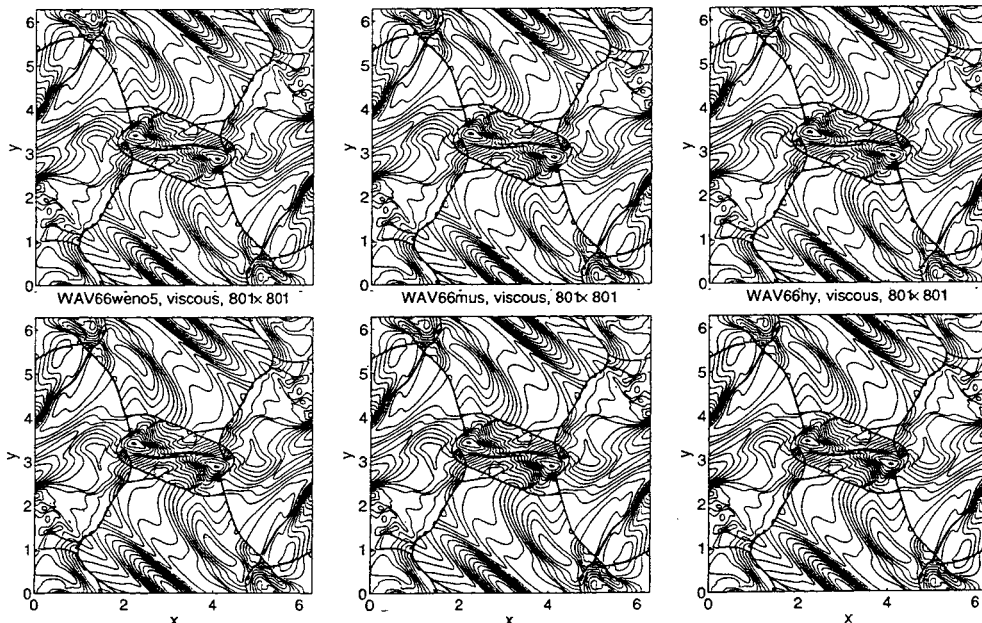

Fig. 4. *Viscous Orszag-Tang Problem using a* 801×801 *grid. Density contours for non-ideal MHD with* $Re = 1000$, *and resistivity coeff. of* 100 *at* $T = 3.14$. *Top row: WENO5(left), MUSCL(middle), HY(right). Bottom row: WAV66weno5(left), WAV66mus(middle), WAV66hy(right).*

For the viscous case, the flow structure is less complicated than that of the inviscid case. All computations use a CFL of 0.6. For coarse grids, again small structures are better captured by the three filter methods than by WENO5, MUSCL and Harten-Yee. For both the inviscid and viscous computations, all three filter methods using the no filter on **B** option are divergence-free preserving. Whereas the "**filter all**" option as well as WENO5, MUSCL and HY are not divergence free. Their $\nabla \cdot \mathbf{B}$ numerical error at $T = 3.14$ increases as the grid is refined.

For this test case, MUSCL and Harten-Yee require similar CPU time. The CPU required by the three filter methods are within 15% depending on the problem, grid spacings and time steps. They require slightly more CPU time (20%) than the Harten-Yee and MUSCL schemes. WENO5 requires at least twice the CPU time of all considered methods.

4.2. A PLANAR SHOCK INTERACTING WITH A MAGNETIC CLOUD ($\gamma = 5/3$, SUPERSONIC INFLOW & OPEN BOUNDARIES)

The second test problem is a planar shock interacting with a magnetic cloud studied in [2]. This is a more challenging problem to simulate due to the stiffness of the flow with rapidly developing complex wave interactions close to the boundaries. The same initial configuration as in [18] is considered here. The computational domain is the square $0 < x < 1$, $0 < y < 1$. A planar shock is initially situated at $x = 0.6$ and moves towards the right.

$$(\rho,\ u,\ v,\ w,\ p,\ B_x,\ B_y,\ B_z)_L = (3.86859,\ 0,\ 0,\ 0,\ 167.345,\ 0,\ 2.1826182,\ -2.1826182),$$

$$(\rho,\ u,\ v,\ w,\ p,\ B_x,\ B_y,\ B_z)_R = (1,\ -11.2536,\ 0,\ 0,\ 1,\ 0,\ 0.56418958,\ -0.56418958).$$

Inside the cloud with center at (0.8,0.5) and radius 0.15, a state of increased density is given by the initial state:

$$(\rho,\ u,\ v,\ w,\ p,\ B_x,\ B_y,\ B_z)_C = (10,\ -11.2536,\ 0,\ 0,\ 1,\ 0,\ 0.56418958,\ -0.56418958).$$

The flow velocity is directed in the negative x-direction, and the cloud will move to the left. The right boundary is supersonic inflow, where the right state is imposed. The other boundaries are open boundaries. Density contours with 50 equidistant contours in log scale from $\log(0.99)$ to $\log(48)$ are used.

Figures 5 and 6 show the comparison among the three filter schemes (WAV66weno5+AD8, WAV66mus+AD8, WAV66hy+AD8, d=0.001 in (3.4)), with the "no filter on B option", WENO5, MUSCL and Harten-Yee using uniform 201 × 201 and 801 × 801 grids for the inviscid MHD. Computations using WAV66weno5, WAV66mus, and WAV66hy (d=0 in (3.4)) are not as stable. Figures 7 and 8 show the corresponding viscous MHD comparison using WAV66weno5, WAV66mus, and WAV66hy (d=0 in (3.4)). For the viscous case, AD8 (i.e., $d \neq 0$) is not necessary as part of the base scheme for a stable solution.

As opposed to the Orszag-Tang problem, in this case, grid convergence was not quite achieved for all six methods using the 801 × 801 grid for the inviscid. For both the viscous and inviscid cases, overall the three filter methods are more accurate than the other three methods. Computations based on a 1601×1601 grid are used as the reference solutions (see Fig. 9). For 51×51 and 101 × 101 grids, small structures are better captured by the three filter methods than WENO5, MUSCL and Harten-Yee. Moreover, among the three filter methods, WAV66hy+AD8 is slightly more accurate on capturing the fine scale structures in most coarse grid cases. It is interesting to see the contrast in the flow structure between the inviscid and viscous converged solutions.

For all three filter methods using the no filter on **B** option, perfect $\nabla \cdot \mathbf{B}$ preservation within machine zero is only obtained up to a certain time ($T = 0.04$). The increase in the norm of $\nabla \cdot \mathbf{B}$ is caused by boundary effects. A SBP difference boundary operator is used [11, 10]. Due to the wide grid stencil of the SBP boundary difference operator in conjunction with the need to use an extrapolation to the outermost open boundary point, $\nabla \cdot \mathbf{B}$ is not preserved. The effect is only seen when the solution is non-trivial on the boundary where complex wave interactions are taking place in both directions of the open boundaries. Although divergence-free preservation by the three filter methods is not possible for $T > 0.04$ by the "no filter on **B**" option, the L^2-norm of $\nabla \cdot \mathbf{B}$ for this option is at least an order of magnitude smaller than the "filter all" option and
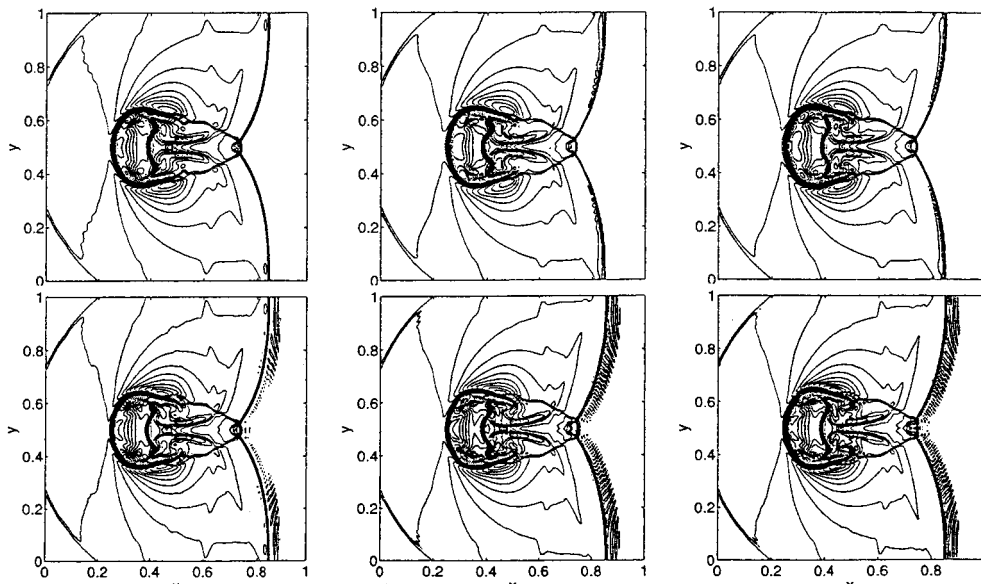
Fig. 5. *Inviscid Magnetic Cloud Problem using a* 201×201 *grid. Density contours for the ideal MHD at* $T = 0.06$. *Top row: WENO5(left), MUSCL(middle), HY(right). Bottom row: WAV66weno5+AD8(left), WAV66mus+AD8(middle), WAV66hy+AD8(right).*
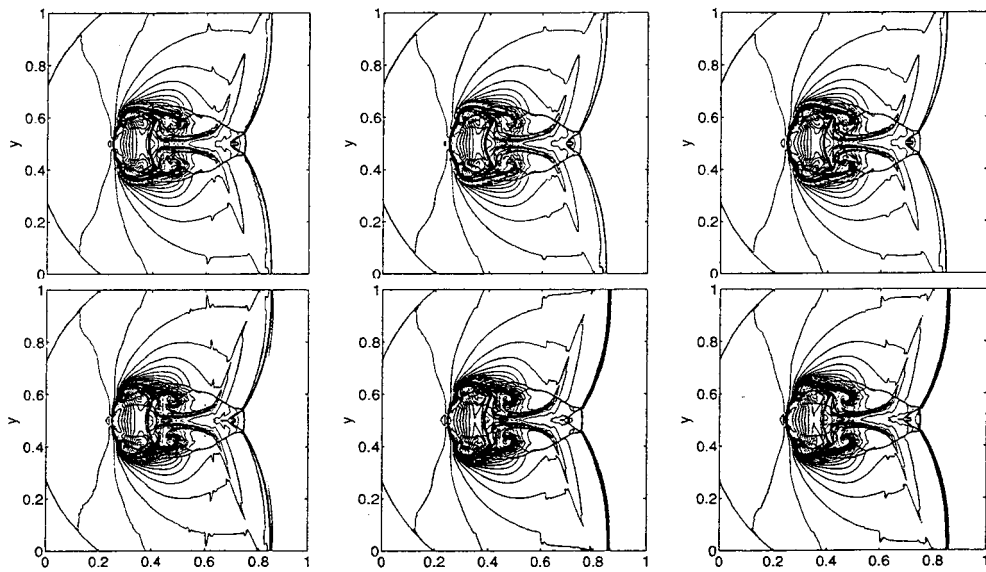

Fig. 6. *Inviscid Magnetic Cloud Problem using a* 801×801 *grid. Density contours for the ideal MHD at* $T = 0.06$. *Top row: WENO5(left), MUSCL(middle), HY(right). Bottom row: WAV66weno5+AD8(left), WAV66mus+AD8(middle), WAV66hy+AD8(right).*

the three standard shock-capturing schemes when $T > 0.04$. See [24, 23] for some illustrations of WAV66hy+AD8. An alternative in obtaining a divergence-free solution is to employ standard divergence free cleaning on the filter step. This is a subject of on going research. The relative CPU required by the six methods are the same as the previous test case.

5. Concluding Remarks

The performance of three nonlinear filters for the adaptive numerical dissipation control in high order methods [20, 16, 17, 24] is investigated. The "no filter on **B**" option by the three filter methods works well for both the conservative and non-conservative (computations not shown) systems and exhibits smaller $\nabla \cdot \mathbf{B}$ numerical error than standard shock-capturing methods without traditional divergence cleanings. For periodic boundary conditions and for open boundaries
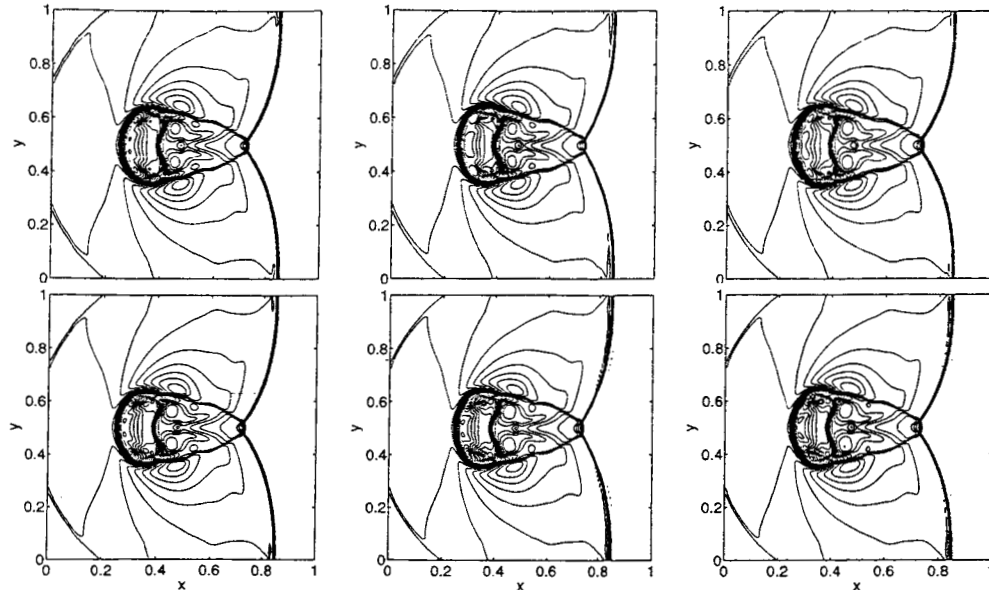
Fig. 7. *Viscous Magnetic Cloud Problem using a* 201×201 *grid. Density contours for non-ideal MHD with* $Re = 1000$, *and resistivity coeff. of* 100 *at* $T = 0.06$. *Top row: WENO5(left), MUSCL(middle), HY(right). Bottom row: WAV66weno5(left), WAV66mus(middle), WAV66hy(right).*
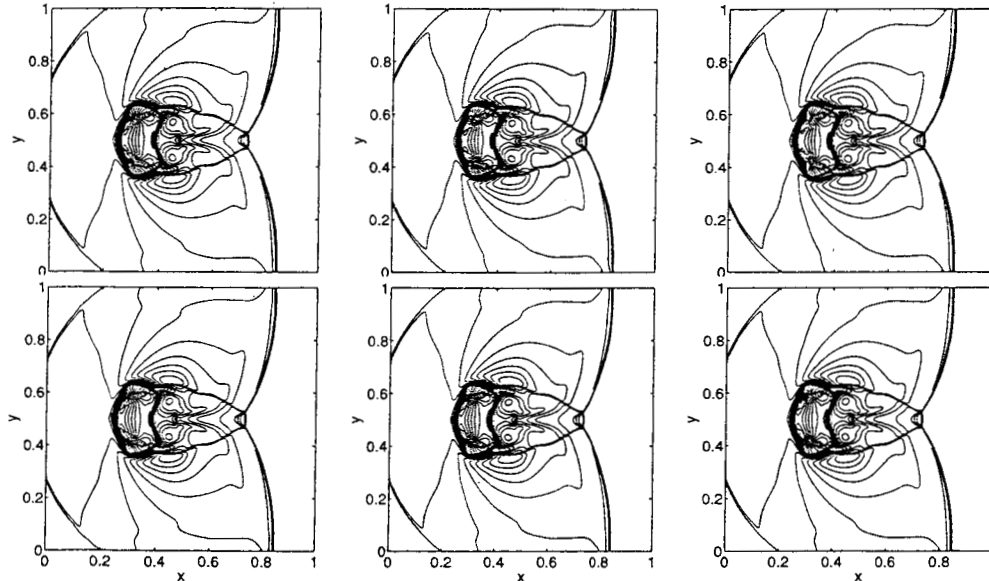

Fig. 8. *Viscous Magnetic Cloud Problem using a* 801×801 *grid. Density contours for non-ideal MHD with* $Re = 1000$, *and resistivity coeff. of* 100 *at* $T = 0.06$. *Top row: WENO5(left), MUSCL(middle), HY(right). Bottom row: WAV66weno5(left), WAV66mus(middle), WAV66hy(right).*
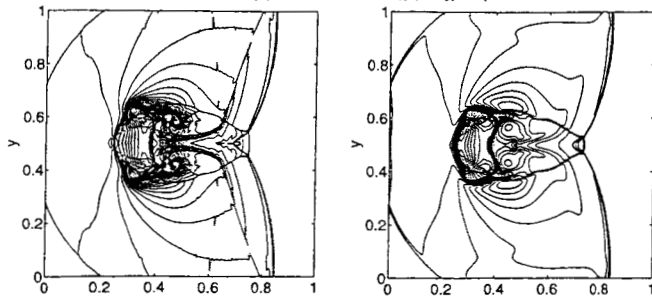

Fig. 9. *Inviscid and Viscous Magnetic Cloud Problem using a* 1601×1601 *grid by WAV66weno5+AD8 (d=0.001). Density contours for ideal and non-ideal MHD with* $Re = 1000$, *and resistivity coeff. of* 100 *at* $T = 0.06$, *inviscid (left) and viscous (right)*

without complex wave interactions near the physical boundaries, these filter schemes are divergence free. In general, for coarse grids, the high order methods are more accurate and require less grid points than required by second-order methods. For fine enough grids, in most test cases, the accuracy is similar for all six methods. Among the three filter methods, WAV66hy+AD8 is slightly more accurate on capturing the fine scale structures in most of the coarse grid cases.

For the two test cases, MUSCL and Harten-Yee require similar CPU time. The CPU required by the three filter methods are within 15% depending on the problem, grid spacings and time steps. They require slightly more CPU time (20%) than the Harten-Yee and MUSCL schemes. WENO5 requires at least twice the CPU time of all other of the methods. This is due to the fact that all filter schemes require only one Riemann solve per time step per direction (independent of the time discretizations of the base scheme step) as opposed to two Riemann solves per time step per direction by the MUSCL, Harten-Yee schemes using a second-order Runge-Kutta method. In addition, for the two test cases and all six methods (except the no filter on **B** option for the three filter schemes), the $\nabla \cdot \mathbf{B}$ numerical errors (at their corresponding stopping times) increase as the grid is refined.

Acknowledgments

References

1. P. Cargo and G. Gallice, *Roe Matrices for Ideal MHD and Systematic Construction of Roe Matrices for Systems of Conservation Laws*, J. Comput. Phys., **136** (1997), pp. 446-466.
2. W. Dai and P. R. Woodward, *A Simple Finite Difference Scheme for Multidimensional Magnetohydrodynamical Equations*, J. Comput. Phys., **142** (1998), pp. 331-369.
3. C.R. Evans and J.F. Hawley, *Simulation of Magnetohydrodynamic Flows: A Constrained Transport Method*, Astrophys. J. **332**, (1988), pp. 659–677.
4. G. Gallice, *Systéme D'Euler-Poisson, Magnétohydrodynamique et Schemeas de Roe*, PhD Thesis, L'Université Bordeaux I, 1997.
5. D.V. Gaitonde, *Development of a Solver for 3-D Non-Ideal Magnetogasdynamics* AIAA Paper 99-3610, 1999.
6. S.K. Godunov *Symmetric Form of the Equations of Magnetohydrodynamics,* Numerical Methods for Mechanics of Continuum Medium, **13**, no. 1 (1972), pp. 26-34
7. A. Harten and J.M. Hyman, *A Self-Adjusting Grid for the Computation of Weak Solutions of Hyperbolic Conservation Laws*, J. Comput. Phys., **50**, (1983), pp. 235–269.
8. G.-S. Jiang and C.-W. Shu, *Efficient Implementation of Weighted ENO schemes*, J. Comput. Phys., **126** (1996), pp. 202–228.
9. H. Nessyahu and E. Tadmor, *Non-oscillatory Central Differencing for Hyperbolic Conservation Laws*, J. Comput. Phys, **87**, pp408-463, 1990.
10. J. Nordstrom and M.H. Carpenter, *Boundary and Interface Conditions for High-Order Finite-Difference Schemes Applied to the Euler and Navier-Stokes Equations,* J. Comput. Phys. 148, (1999), pp. 621-645.
11. P. Olsson, *Summation by Parts, Projections and Stability, I.* Math. Comp. **64**, (1995), pp. 1035-1065.
12. S.A. Orszag and C.M. Tang *Small-Scale Structure of Two-Dimensional Magnetohydrodynamic Turbulence,* J. Fluid Mech., **90**, (1979), pp. 129–143.
13. J.M. Picone and R.B. Dahlburg, *Evolution of the Orszag-Tang Vortex System in a Compressible Medium. II. Supersonic Flow,* Phys. Fluid B, **3**, (1991), pp. 29-44.
14. K.G. Powell, *An Approximate Riemann Solver for Magnetohydrodynamics (That works in More than One Dimension)*, ICASE-Report 94-24, NASA Langley Research Center, April 1994.
15. B. Sjögreen, *High Order Centered Difference Methods for the Compressible Navier-Stokes Equations*, J. Comput. Phys., **117**, (1995), pp. 67-78.
16. B. Sjögreen and H. C. Yee, *Multiresolution Wavelet Based Adaptive Numerical Dissipation Control for Shock-Turbulence Computation,* RIACS Technical Report TR01.01, NASA Ames research center (Oct 2000); also, J. Scient. Computing, **20**, (2004), pp. 211-255.
17. B. Sjögreen and H.C. Yee, *Efficient Low Dissipative High Order Schemes for Multiscale MHD Flows, I: Basic Theory,* AIAA 2003-4118, Proceedings of the 16th AIAA/CFD Conference, June 23-26, 2003, Orlando, Fl.
18. G. Tóth, *The div B=0 Constraint in Shock-Capturing Magnetohydrodynamic Codes,* J. Comput. Phys., **161**, (2000), pp. 605-652.
19. H.C. Yee, *A Class of High-Resolution Explicit and Implicit Shock-Capturing Methods,* VKI Lecture Series 1989-04, March 6-10, 1989, also NASA TM-101088, Feb. 1989.

20. H.C. Yee, N.D. Sandham, N.D., and M.J. Djomehri, *Low Dissipative High Order Shock-Capturing Methods Using Characteristic-Based Filters*, J. Comput. Phys., **150** (1999) pp. 199-238.

21. H.C. Yee, M. Vinokur, M., and M.J. Djomehri, *Entropy Splitting and Numerical Dissipation*, J. Comput. Phys., **162** (2000) pp. 33-81.

22. H.C. Yee and B. Sjögreen, *Designing Adaptive Low Dissipative High Order Schemes for Long-Time Integrations*, **Turbulent Flow Computation**, (Eds. D. Drikakis & B. Geurts), Kluwer Academic Publisher (2002); also RIACS Technical Report TR01-28, Dec. 2001.

23. H.C. Yee and B. Sjögreen, *Divergence Free High Order Filter Methods for the Compressible MHD Equations*, Proceedings of the International Conference on High Performance Scientific Computing, March 10-14, 2003, Hanoi, Vietnam.

24. H.C. Yee and B. Sjögreen, *Efficient Low Dissipative High Order Scheme for Multiscale MHD Flows, II: Minimization of Div(B) Numerical Error*, RIACS Technical Report TR03.10, July 2003, NASA Ames Research Center.

25. H.C. Yee and B. Sjögreen, *Adaptive Numerical Dissipation Control in High Order Schemes for 3-D Non-Ideal MHD*, Proceedings of the ICCFD3, July 12-16, 2004, Toronto, Canada.

26. A.L. Zachary, A. Malagoli, and P. Colella, *A Higher-Order Godunov Method for Multidimensional Ideal Magnetohydrodynamics*, SIAM J. Sci. Comput., **15**, (1994), pp. 263-284.